SPITZER OBSERVATIONS OF YOUNG RED QUASARS

TANYA URRUTIA[1], MARK LACY[2], HENRIK SPOON[3], EILAT GLIKMAN[4], ANDREEA PETRIC[5], AND BERNHARD SCHULZ[6]

[1] Leibniz Institut für Astrophysik Potsdam, An der Sternwarte 16, D-14482 Potsdam, Germany; turrutia@aip.de
[2] NRAO, 520 Edgemont Road, Charlottesville, VA 22903, USA; mlacy@nrao.edu
[3] Department of Astronomy, Cornell University, 219 Space Sciences Building, Ithaca, NY 14853, USA; spoon@isc.astro.cornell.edu
[4] Department of Physics, Yale University, P.O. Box 208120, New Haven, CT 06520, USA; eilat.glikman@yale.edu
[5] Astronomy Department, California Institute of Technology, Pasadena, CA 91125, USA; ap@astro.caltech.edu
[6] Infrared Processing and Analysis Center, California Institute of Technology, MC 100-22, Pasadena, CA 91125, USA; bschulz@ipac.caltech.edu
Received 2012 February 10; accepted 2012 July 17; published 2012 September 11

ABSTRACT

We present mid-infrared spectra and photometry of 13 redshift $0.4 < z < 1$ dust reddened quasars obtained with *Spitzer* IRS and MIPS. We compare properties derived from their infrared spectral energy distributions (intrinsic active galactic nucleus (AGN) luminosity and far-infrared luminosity from star formation) to the host luminosities and morphologies from *Hubble Space Telescope* imaging, and black hole masses estimated from optical and/or near-infrared spectroscopy. Our results are broadly consistent with models in which most dust reddened quasars are an intermediate phase between a merger-driven starburst triggering a completely obscured AGN, and a normal, unreddened quasar. We find that many of our objects have high accretion rates, close to the Eddington limit. These objects tend to fall below the black hole mass–bulge luminosity relation as defined by local galaxies, whereas most of our low accretion rate objects are slightly above the local relation, as typical for normal quasars at these redshifts. Our observations are therefore most readily interpreted in a scenario in which galaxy stellar mass growth occurs first by about a factor of three in each merger/starburst event, followed sometime later by black hole growth by a similar amount. We do not, however, see any direct evidence for quasar feedback affecting star formation in our objects, for example, in the form of a relationship between accretion rate and star formation. Five of our objects, however, do show evidence for outflows in the [O III]5007 Å emission line profile, suggesting that the quasar activity is driving thermal winds in at least some members of our sample.

Key words: infrared: galaxies – galaxies: evolution – galaxies: starburst – quasars: general

Online-only material: color figures

1. INTRODUCTION

The study of quasars across cosmic time has proven to be important as their evolution and growth is intimately linked to that of their host galaxy. Mergers have long been invoked as the primary ignition mechanism of quasar activity, at least for the high-luminosity objects (Sanders & Mirabel 1996; Urrutia et al. 2008; Bennert et al. 2008). The loss of angular momentum during a gas-rich merger allows the gas to be funneled to the center igniting a starburst and fueling the central black hole. In this model, eventually the quasar grows strong enough and develops a feedback mechanism that expels the obscuring material and shuts off star formation (Silk & Rees 1998; Hopkins et al. 2008). This scenario is further supported by the existence of tight correlations between the properties of galaxy bulges and their central black holes (Magorrian et al. 1998; Ferrarese & Merritt 2000).

Putting the picture together observationally is challenging, however. Populations of quasars selected via different techniques, although overlapping, differ substantially in their detailed properties and may bias toward a particular type of quasar or evolutionary phase e.g., active galactic nuclei (AGNs) selected in the infrared may belong to different class or evolutionary phase than AGNs selected in the radio or optical regime (Hickox et al. 2009). In an ideal survey, we would be able to select quasars at specific points in their lifetimes. For example, to test a starburst–AGN connection we would prefer to select young, recently ignited objects to see if there is still star formation occurring in the host galaxies and to identify likely feedback mechanisms.

One approach to finding candidates for young quasars is to search for dust obscured quasars that may correspond to objects yet to fully clear out the dust and gas surrounding them. Conventionally, obscured quasars are divided into two classes: (1) the so-called type-2 quasars—objects showing only narrow emission lines with large inferred extinctions ($A_V > 5$–100) toward the nucleus, most likely caused by a torus surrounding the accretion disk as required in the AGN "unification by orientation" model (e.g., Antonucci 1993; Urry & Padovani 1995) and (2) moderately reddened quasars ($A_V \sim 1$–5), which still show broad emission lines in the rest-frame optical, and whose continuum is still dominated by the quasar rather than the host galaxy. These latter objects are obscured by a cold absorber along the line of sight to the quasar, most likely in the host galaxy. They may thus represent the young objects in the final stages of emerging from their dusty cocoons. Throughout this paper the terms red, dust obscured, and moderately reddened quasars all refer to the latter category of objects.

Dust obscured quasars of all types are missing from, or are severely underrepresented in optical surveys, but are present in the radio (e.g., White et al. 2003), in the X-ray (e.g., Hickox et al. 2007), when selected on the basis of narrow optical AGN emission lines (Zakamska et al. 2003), or when selected in the near-infrared (Cutri et al. 2001). Mid-infrared surveys (e.g., Lacy et al. 2004, 2007a; Stern et al. 2005; Alonso-Herrero et al. 2006; Donley et al. 2007) have also been extremely successful at finding and identifying obscured quasars over a wide range of reddenings, redshifts, and luminosities. Surveys combining deep radio and mid-infrared data show that the optically and/or X-ray-selected quasar population constitutes less than half of

the total population of quasars (Donley et al. 2005; Martínez-Sansigre et al. 2005). Joint selection using radio and near-infrared, as used for the sample in this paper, has proven to be one of the most reliable ways to select the moderately obscured quasar population. The requirement of a bright radio source and very red optical through near-infrared colors results in a set of candidates with relatively little contamination from normal galaxies, low-luminosity AGNs, and stars (Gregg et al. 2002; Lacy et al. 2002; Glikman et al. 2004, 2007, 2012; Urrutia et al. 2009).

The success of the *Spitzer Space Telescope* (Werner et al. 2003) has allowed for the detailed study of quasars in the mid-infrared. Programs with the Infrared Spectrograph (IRS; Houck et al. 2004), in particular, have refined our knowledge of QSO spectral energy distributions (SEDs) in the mid-infrared. For example, the detection of silicate in emission in IRS spectra of quasars is a strong support for the unification model (Hao et al. 2005; Siebenmorgen et al. 2005). Average properties of classes of objects using IRS spectra (e.g., Spoon et al. 2007) have allowed us to constrain the physical properties of dust in AGNs (e.g., Nikutta et al. 2009). On average the spectra of luminous quasars are flat, show little or no polycyclic aromatic hydrocarbon (PAH) emission and the silicate features are in emission, associated with dust re-emission. In contrast, the spectra of ultraluminous infrared galaxies (ULIRGs) show a steep rise toward the long wavelengths, moderate PAH emission, and silicate absorption troughs associated with embedded star formation (Hao et al. 2007). However, some type-2 and some reddened quasars at moderate to high redshifts show deep silicate absorption features (Lacy et al. 2007b; Martínez-Sansigre et al. 2008; Zakamska et al. 2008) in contrast to samples of X-ray-selected type-2 quasars, in which they are generally weak (Sturm et al. 2006).

The Multiband Imaging Photometer for SIRTF (MIPS; Rieke et al. 2004) on board *Spitzer* has also allowed us to sample the colder part of the galaxy SED. While AGNs dominate the bright $24\,\mu$m population (Donley et al. 2008), the *Spitzer* $70\,\mu$m field population is dominated by ULIRGs which have a high merger fraction (Kartaltepe et al. 2010a, 2010b). However, AGNs and quasars still make up a significant fraction of $70\,\mu$m sources, and high star formation rates in quasar hosts are common (e.g., Schweitzer et al. 2006; Netzer et al. 2007). Consistent with those results Shi et al. (2009) find that type-1 quasars show star formation rates higher than the field galaxies, with luminosities typical of luminous infrared galaxies (LIRGs; $L_{IR} = 10^{11-12}\,L_\odot$). In particular, dust reddened quasars have been found to have higher than usual $60/12\,\mu$m luminosity ratios, an indicator of higher star formation rates (Georgakakis et al. 2009).

In this paper, we will describe *Spitzer* IRS and MIPS observations of 13 redshift $0.4 < z < 1$ reddened quasars selected using joint radio and near-infrared selection for which we have also obtained *Hubble Space Telescope* (*HST*) observations (Urrutia et al. 2008). We use these observations to estimate the intrinsic luminosities of the quasars and to estimate or constrain the star formation rates in the host galaxies. We then evaluate the evidence that this population corresponds to an intermediate stage in quasar evolution by estimating black hole masses and accretion rates, comparing our *HST* host galaxy luminosities and morphologies to the other properties, and by searching for evidence of feedback processes at work in the hosts. Throughout this paper we adopt a flat universe, $H_0 = 70$ km s^{-1} Mpc^{-1} and $\Omega_\Lambda = 0.7$ cosmology.

2. QUASAR SAMPLE AND OBSERVATIONS

In the past few years we have been selecting a sample of luminous lightly obscured quasars using a combination of the Faint Images of the Radio Sky at Twenty-Centimeters (FIRST) radio survey (Becker et al. 1995), the Two Micron All Sky Survey (2MASS) near-infrared survey (Skrutskie et al. 2006), and the Cambridge Automated Plate Measuring Machine (APM) scans of the POSS plates. Using a $J - K > 1.7$ and $R - K > 4$ color wedge for the matched point sources, we have been very effective in finding these so-called red quasars with spectroscopic follow up at Keck (ESI) and IRTF (Spex) (Glikman et al. 2004, 2007; Urrutia et al. 2009). Even though the survey is radio selected, most of the objects rather fall in the radio intermediate regime than radio loud, so it is unlikely that the redness of the objects comes from a synchrotron component, but is in fact associated with dust reddening. Furthermore, the excess of steep spectrum sources at faint radio fluxes and the point-source nature of the radio sources leads us to expect that the nature of the radio emission is due to a quasar and not from star formation (Glikman et al. 2007). As of early 2012, we have well over 120 spectroscopically confirmed red quasars found with this method (Glikman et al. 2012).

These red quasars are highly luminous and only moderately reddened ($A_V \sim 1$–5 mag), so they outshine their host galaxies in the rest-frame optical and are thus not red due to galaxy starlight. Their SEDs are generally well fit by reddening a standard quasar template spectrum using a Small Magellanic Cloud (SMC) dust-reddening law. It is only in the rest-frame UV, where the quasar light is heavily extinguished, that the host galaxy starts to play a role in terms of overall flux density. See Glikman et al. (2007) and Urrutia et al. (2009) for in-depth discussions of how reddening is estimated for these objects.

A representative sample of 13 dust reddened quasars with $0.4 < z < 1$ were followed up with the Advanced Camera for Surveys (ACS) Wide Field Camera on *HST* with the F475W and F814W filters. These are very luminous quasars at $z \sim 0.7$ having intrinsic absolute magnitudes in the range $-23.5 \geqslant M_B \geqslant -26.2$. The host galaxies show a high amount of interaction: 85% of the images show evidence of morphological disturbance (Urrutia et al. 2008). We also observed that the more reddened the objects were, the more disturbed their morphologies (as measured by the Gini coefficient combined with the concentration index; Lotz et al. 2004; Abraham et al. 2003). These results support the merger-induced origin for high-luminosity quasars.

We followed up this sample of 13 red quasars with the MIPS and IRS on board the *Spitzer Space Telescope* (PID 40143). The IRS observations were made with the short–low (SL; $\Delta\lambda = 5.2$–$14.5\,\mu$m) and long–low (LL; $\Delta\lambda = 14.0$–$38.0\,\mu$m) modules of the IRS, (with some of the highest redshift objects not using the SL2 5–$7.5\,\mu$m module). We also obtained MIPS $24\,\mu$m, $70\,\mu$m, and $160\,\mu$m photometry (with the lowest redshift objects not being observed at $160\,\mu$m). Table 1 provides the details for our *Spitzer* observations, including the IRS and MIPS AORIDs as well as the MIPS 24, 70, and $160\,\mu$m fluxes.

Our infrared spectra and photometry were used for a number of purposes. We can infer star formation rates from the PAH emission in the IRS spectra and the far-infrared excesses from the MIPS photometry. The silicate feature at $9.7\,\mu$m provides us with an estimate of the cold dust obscuration, and the mid-infrared continuum emission provides an estimate of the intrinsic (unreddened) quasar luminosity. Near-infrared and optical spectra of these objects are shown in Glikman et al.

Table 1
Spitzer IRS and MIPS Observations

Source	IRS AORID	MIPS AORID	S_{24} (mJy)	S_{70} (mJy)	S_{160} (mJy)
F2M0729+3336	22386176	22386432	12.9 ± 3.0	<15	<30
F2M0825+4716	22389760	22386688	36.1 ± 4.7	85 ± 19	46 ± 11
F2M0830+3759	22390016	22386944	26.1 ± 3.9	32 ± 12	<30
F2M0834+3506	22390272	22387200	17.6 ± 3.4	26 ± 13	<30
F2M0841+3604	22390528	22390528	11.7 ± 3.0	53 ± 14	<30
F2M0915−2418	17540352[a]	22387712	87.3 ± 7.0	207 ± 24	73 ± 12
F2M1012+2825	22390784	22387968	4.9 ± 0.8	<15	<30
F2M1113+1244	22391040	22388224	59.4 ± 5.8	138 ± 25	67 ± 12
F2M1118−0033	22391296	22388480	24.4 ± 4.0	80 ± 24	44 ± 10
F2M1151+5359	22391552	22388736	6.9 ± 0.7	20 ± 7	<30
F2M1507+3129	22391808	22388992	9.2 ± 2.5	22 ± 11	<30
F2M1532+2415	22392064	22389248	28.4 ± 4.0	31 ± 13	<30
F2M1656+3821	22392320	22389504	9.7 ± 2.4	15 ± 8	<30

Notes. [a] All observations made in cycle 4 (2007 July–2008 May) except for F2M0915−2418, whose IRS spectrum was taken in 2007 May as part of program 30121.

(2004, 2007), though we obtained an additional spectrum of FTM1507+3129, see Section 4.1.11.

3. DATA REDUCTION AND ANALYSIS

The IRS spectra were reduced in the following manner. First, we removed the bad or hot pixels using the IDL program `irsclean`. The resulting spectra were background subtracted by differencing the first- and second-order apertures. They were then extracted and flux calibrated using SPICE version 2.0.1 provided by the Spitzer Science Center. Finally, the different orders were stitched together using a weighted average in the overlapping orders, with no significant scaling adjustments needed in the order-to-order jumps. A plot of the 13 different normalized spectra can be seen in Figure 1.

We used the post-BCD products for the 24 μm MIPS images, as the quality was excellent and there was no need to re-mosaic them. For the 70 and 160 μm data, we re-mosaiced the data using `MOPEX` version 18.2.2 with the default parameters. We employed two methods for the photometric measurements: (1) The `APEX` package within `MOPEX` with the default parameters and point response function for point-source photometry and (2) `SExtractor` aperture photometry with standard point-source aperture corrections provided by the Spitzer Science Center.[7] We used 10% errors for the 70 and 160 μm sources, as `MOPEX` tended to underestimate the errors.

3.1. IRS Spectral Analysis

For all the IRS spectra in our sample we measured the equivalent width (EW) of the 6.2 μm PAH emission as well as the strength of the 9.7 μm silicate absorption feature following the methodology presented in Spoon et al. (2007). In short, the PAH EW is obtained by integrating above a spline interpolated continuum, while the silicate feature strength is inferred from the ratio between the observed and continuum flux density:

$$S_{\mathrm{Sil}} = \ln \frac{f_{\mathrm{obs}}(9.7\,\mu\mathrm{m})}{f_{\mathrm{cont}}(9.7\,\mu\mathrm{m})}. \qquad (1)$$

The values are given in Table 2 and plotted in Figure 2. We discuss the results in the diagram in Section 4.
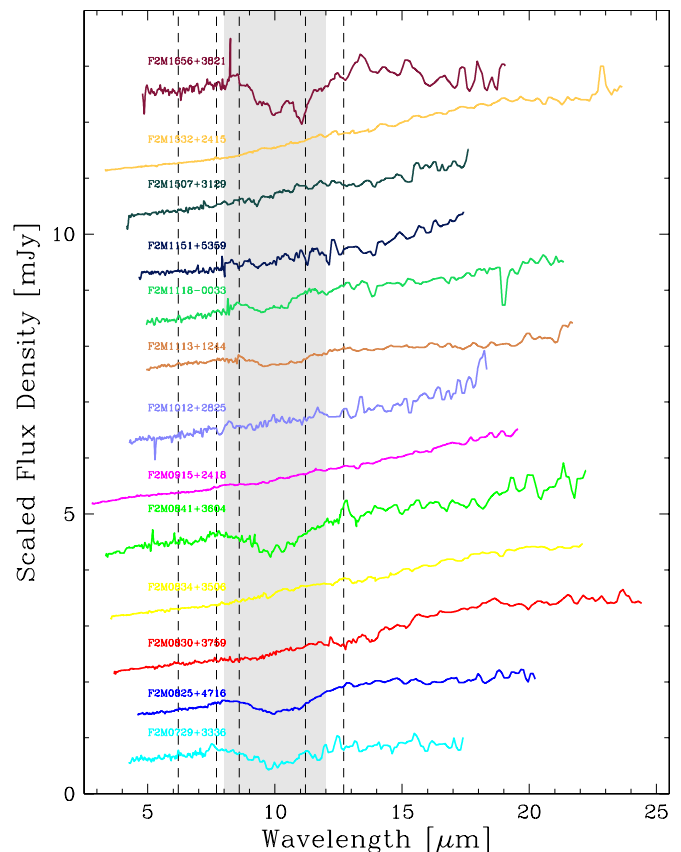

Figure 1. Stacked IRS rest-frame spectra of red quasars. The spectra are normalized to 1 at 15 μm and offset. The dashed lines denote the central wavelengths of the family of PAH emission features at 6.2, 7.7, 8.6, 11.2, and 12.7 μm. The shaded region represents the typical region (8.0–12.0 μm) where the 9.7 μm silicate absorption feature is seen.

(A color version of this figure is available in the online journal.)

3.2. Multiwavelength Modeling

To obtain a complete view of the physical phenomena that are affecting the quasar, we modeled the SEDs of our sample from the optical out to the mid-infrared. We used the
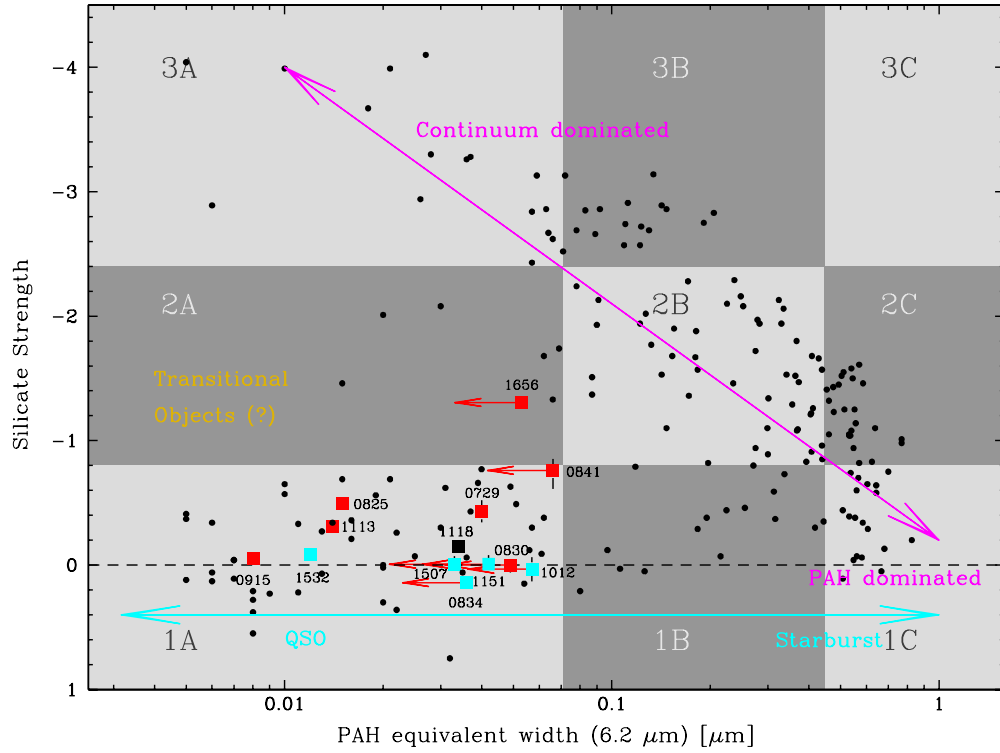
---

[7] Using the old Web site, http://ssc.spitzer.catech.edu/mips/apercorr, values can now be found in the MIPS instrument handbook at http://ssc.spitzer.caltech.edu/mips/mipsinstrumenthandbook/50/

Figure 2. Diagnostic diagram of Spoon et al. (2007) with their sources plotted as small filled circles. Our quasars are plotted as larger squares with the PAH values showing arrows being upper limits. Usually sources cluster along two tracks: the diagonal continuum track from 1C to 3A (magenta) spanning from starburst to ULIRG-type systems and the activity track from 1A to 1C (cyan) spanning from QSOs to starburst galaxies. Most of the quasars are found in quadrant 1A, but some have silicate troughs deep enough to be in quadrant 2A, which Spoon et al. (2007) speculates to be transitional objects.

(A color version of this figure is available in the online journal.)

Table 2
Parameter Results from Multiwavelength Fitting

Source	QSO Contribution (Intrinsic) (log $L_{\rm QSO}/L_\odot$)	Starburst (FIR) Contribution (log $L_{\rm FIR}/L_\odot$)	QSO/SB Ratio	$E(B-V)$[a] (Spectrum)	$E(B-V)$[b] (SED Fit)	$S_{\rm Sil}$	D[c] Coefficient
F2M0729+3336	12.83	<11.47	>22.91	0.83 ± 0.22	0.605	-0.43 ± 0.09	1.92
F2M0825+4716	13.10	12.35	5.62	0.52 ± 0.10	0.806	-0.50 ± 0.03	1.29
F2M0830+3759	12.03	11.35	4.79	0.80 ± 0.15	0.478	0.00 ± 0.06	1.39
F2M0834+3506	12.04	11.42	4.17	0.58 ± 0.05	0.629	0.14 ± 0.03	0.95
F2M0841+3604	12.12	12.03	1.23	1.34 ± 0.11	0.770	-0.76 ± 0.15	1.73
F2M0915−2418	13.37	12.69	4.79	0.36 ± 0.12	0.354*	-0.05 ± 0.05	1.29
F2M1012+2825	12.24	<11.88	>2.29	0.82 ± 0.10	0.647	0.03 ± 0.10	1.13
F2M1113+1244	13.14	12.43	5.13	1.41 ± 0.11	0.294	-0.31 ± 0.01	1.24
F2M1118−0033	12.71	12.29	2.63	0.85 ± 0.11	0.512	-0.15 ± 0.04	1.40
F2M1151+5359	12.15	11.77	2.40	0.42 ± 0.08	0.532*	-0.01 ± 0.07	0.95
F2M1507+3129	12.57	12.05	3.31	0.74 ± 0.09	0.532*	-0.01 ± 0.07	1.16
F2M1532+2415	12.47	10.67	63.10	0.90 ± 0.53	0.354*	-0.09 ± 0.02	1.50
F2M1656+3821	12.44	10.83	40.74	0.88 ± 0.16	1.169	-1.31 ± 0.01	1.34

Notes.
[a] Derived via spectral fitting of a quasar composite reddened by the SMC law, either from Urrutia et al. (2008) or Urrutia et al. (2009); the latter involves much more careful fitting, masking emission line regions.
[b] Derived from the SED fitting and modeling as described in Section 3.2, the extinction (τ_V) is derived from silicate absorption, except for objects marked with a star. Note the general agreement with the silicate depth derived via the method of Spoon et al. (2007).
[c] $D = G/C$, used as disturbance parameter. Values of G and C are from Urrutia et al. (2008), see that publication for details on how the values were obtained. D values close to 1.0 represent morphologically undisturbed systems. The higher the D value, the more disturbed the system is.

available u-, g-, r-, i-, z-band SDSS photometry[8] in the optical. In addition, we used 2MASS (Skrutskie et al. 2006), WISE Band 1+2 (Wright et al. 2010), our MIPS photometry and IRS mid-IR spectra.

To model the SEDs we used a phenomenological model based on that of Sajina et al. (2006) due to the current lack of a good physical understanding of the nature and geometry of the dust emitting regions. Many of the parameters thus do not have a

---

[8] Except for F2M0729+3336, which has no SDSS coverage. We obtained synthetic photometry corresponding to the SDSS filters from the optical spectrum.
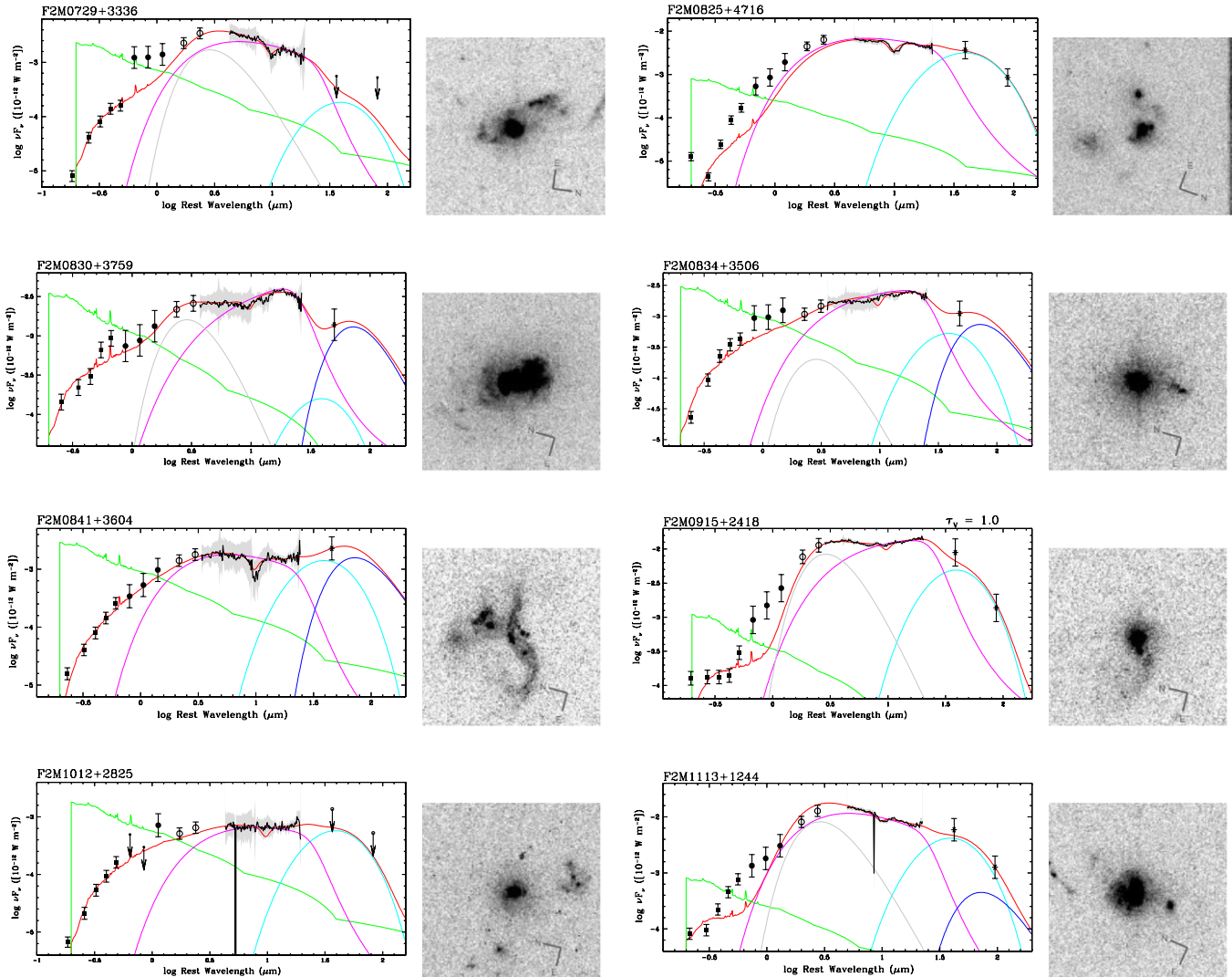
Figure 3. Broadband rest-frame spectral energy distributions (SEDs) of the red quasars. The five photometry measurements from the SDSS are shown as squares, the ones from 2MASS as filled circles, the ones from WISE Band 1+2 as open circles, and the ones from MIPS as stars (three of the low-redshift quasars were not observed at MIPS 160 μm). Also shown is the IRS spectrum with a corresponding gray error area. The fitted SEDs of the quasars are shown in red. They are builtup from a quasar component (in green) and AGN hot dust component (pink), both of which are reddened by an SMC extinction law. Furthermore a very hot quasar dust component (gray), a warm dust component (cyan), and a cold dust component (blue) are added. The corresponding *HST* image is shown to the right of each SED as an 7×7 arcsec gray-scale image.

(A color version of this figure is available in the online journal.)

direct physical interpretation. Nevertheless, we considered the effort worthwhile as it allows an empirical breakdown of the contributions of starlight, hot dust emission from the AGN, and cooler dust emission from star formation. The model fits are shown in Figure 3. Full details of the model components as applied to quasars are given in Hiner et al. (2009), but are summarized below.

1. The composite quasar spectrum. As the composite of Vanden Berk et al. (2001) suffers from noticeable host galaxy contamination at the long wavelength end, we constructed a new composite by subtracting the continuum from the composite of Vanden Berk et al. (2001) and adding the residual emission line composite to a new continuum constructed using line-free optical/near-infrared SED points from the composite of Richards et al. (2006). In Figure 3 this is the green line.

2. A power-law component for the mid-infrared emission, with an exponential cutoff at short wavelengths to represent

dust sublimation, and a Fermi function cutoff at long wavelengths. The functional form used was

$$L_{\text{AGN}} = \frac{L_{\text{AGN}}^0 \, \nu^{(1-\alpha)} \, e^{h\nu/k_B T_{\text{sub}}}}{e^{(\nu-\nu_{\text{hcut}})/w} + 1}, \qquad (2)$$

where the normalization, L_{AGN}^0, power-law index α, and T_{sub} (a proxy for the sublimation temperature) are allowed to vary, and ν_{hcut} and w were fixed at 0.11×10^{14} Hz and 0.017×10^{14} Hz, respectively (h and k_B are the Planck and Boltzmann constants, respectively). This component is represented by the magenta line in Figure 3. After addition, components (1) and (2) were reddened by the Galactic Center extinction curve of Chiar & Tielens (2006) to fit any silicate absorption feature.

3. A warm dust component to represent the small grain emission from H II regions, represented by a power law
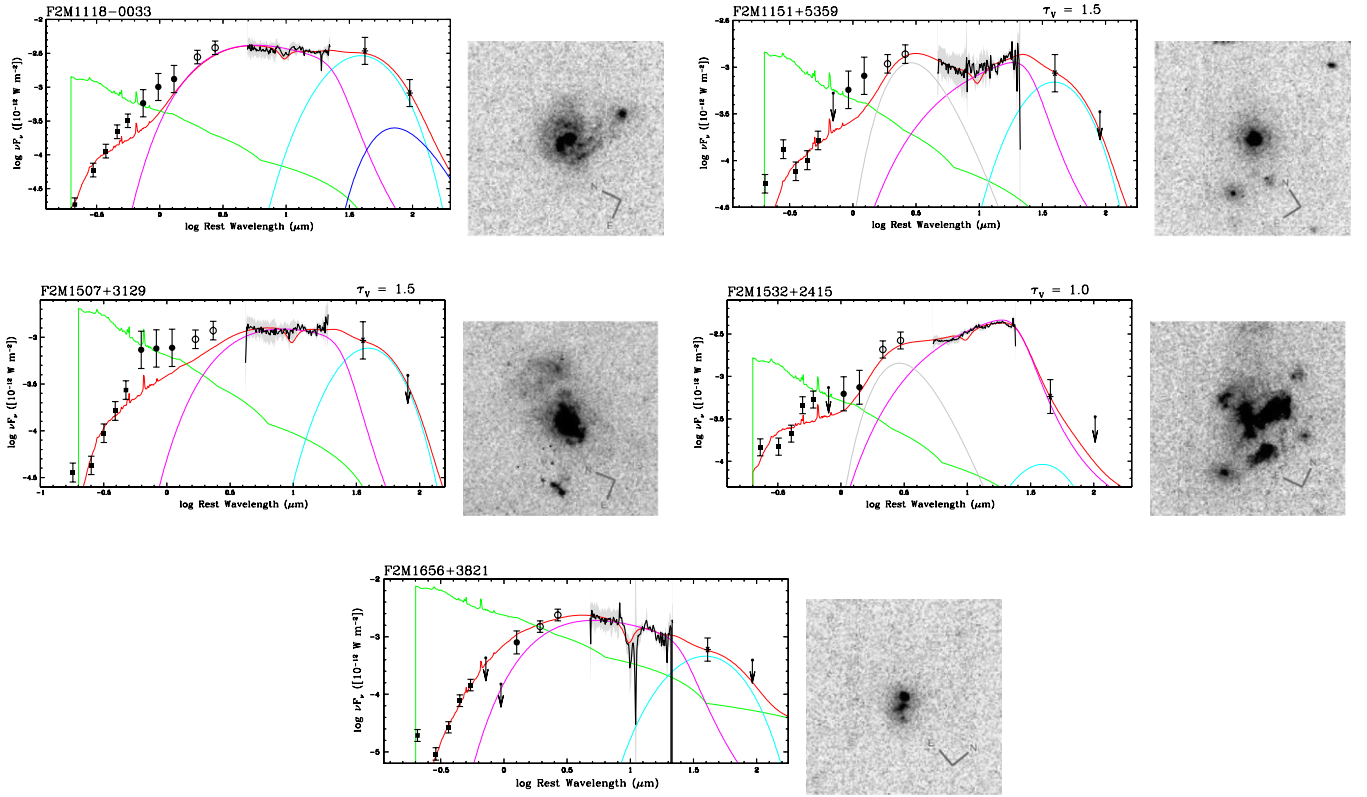
Figure 3. (Continued)

with fixed high- and low-frequency cutoffs:

$$L_{SG} = \frac{L_{SG}^0 \, \nu^{(1-\gamma)} \, e^{-\nu/\nu_{sgl}}}{e^{-\nu_{sgh}/\nu}} \qquad (3)$$

this component is poorly constrained in most of the fits, so γ was fixed at a typical value of two (e.g., Sajina et al. 2006). The high- and low-frequency cutoffs, ν_{sgl} and ν_{sgh} were set to 0.062×10^{14} Hz and 0.17×10^{14} Hz, respectively. Figure 3 shows this component in light blue.

4. A thermal gray-body model for the far-infrared emission:

$$L_{FIR} = \frac{L_{FIR}^0 \, \nu^{3+\beta}}{e^{h\nu/k_B T} - 1}. \qquad (4)$$

For all of the objects, we fixed the temperature of this component, T, to 40 K, because of the uncertainty in our $160\,\mu m$ photometry. β was fixed at 2.0 as above (Dunne & Eales 2001). In Figure 3, this is represented with a dark blue line.

5. Many quasars objects also required an extra near-infrared component to match the SEDs. This "very hot" component was modeled as a 1000 K blackbody (Equation (4) with $T = 1000$). The physical origin of this component is unclear, but it is most likely due to hot dust close to the sublimation radius (e.g., Glikman et al. 2006; Netzer et al. 2007; Mor & Trakhtenbrot 2011). This last component can be seen in gray color in Figure 3.

In addition, we tried to add a PAH model as described in Lacy et al. (2007b); however, PAH emission was relatively minimal and did not improve our fits. We therefore excluded this component in the fitting process. The contribution from starlight is so small compared to the quasar and star formation

components at all wavelengths except blueward of ≈ 5000 Å, so we decided to ignore the stellar contribution in our fitting process.

Most of our quasars are well fit by this model, with relatively small χ^2/dof values, but in some cases the fit at the near-IR regions of the spectrum described by 2MASS magnitudes provides is poor. This is most likely due to the host galaxy emission dominating the optical and/or near-infrared passbands.

In the cases where the model fit the broadband SED well, the reddening values derived from the silicate absorption feature were in general agreement to the values of $E(B-V)$ derived from the SMC continuum fit to the optical spectrum (Glikman et al. 2007; Urrutia et al. 2009), confirming cold dust as the absorbing and reddening mechanism in these systems (see Table 2). However, in four cases (F2M0915+2418, F2M1151+5359, F2M1507+3129, and F2M1532+2415) there was no silicate in absorption to account for the reddening seen in the optical and near-infrared. In those cases, we artificially fixed the extinction τ_V that would have been derived from the fit from the IRS spectrum manually. These objects have their modeled extinctions marked with a star in Table 2 and their fixed extinctions labeled in Figure 3.

We then derived the obscured quasar luminosities by integrating over the quasar components (1)+(2); the intrinsic luminosities quoted in Table 2 are then derived by accounting for the extinction obtained from the silicate absorption fit. Since the AGN contribution is well constrained by the IRS spectrum and optical/near-IR photometry points, the uncertainties are overall small ($\lesssim 0.2$ dex) and only pertain to the accuracy of the silicate absorption feature. The FIR/starburst contribution was taken solely from the integration of the two dust bumps (light and dark blue; (3)+(4)), not from any component in the optical regime. Since that FIR contribution is largely determined by

Table 3
Black Hole Mass Estimates and Eddington Rates

Object	Redshift	Line	FWHM (km s^{-1})	log (νL_{15}) (erg s^{-1})[a]	log ($M_{BH}/M_{\odot}$)	log (L/L_{Edd})	$\log_{10}$ ($L_B/L_{\odot}$) (Fit)[b]	$\log_{10}$ ($L_B/L_{\odot}$) (Monotonic)[c]
F2M0729+3336	0.957	Hβ	2866 ± 200	45.8	8.7 ± 0.1	0.1 ± 0.1	11.06	10.99
F2M0825+4716	0.803	Paβ	2664 ± 100	46.1	8.8 ± 0.1	0.3 ± 0.1	10.30	10.90
F2M0830+3759	0.414	Hβ	3741 ± 200	45.3	8.6 ± 0.1	-0.4 ± 0.1	10.97	11.01
F2M0834+3506	0.470	Hα	10500 ± 2000	45.2	9.5 ± 0.1	-1.3 ± 0.1	10.69	10.65
F2M0841+3604	0.553	Hα	3380 ± 500	45.2	8.5 ± 0.1	-0.4 ± 0.1	10.53	10.73
F2M0915+2418	0.842	Paβ	4186 ± 800	46.5	9.4 ± 0.2	0.1 ± 0.1	10.58	10.66
F2M1012+2825	0.937	Hα	8050 ± 1000	45.3	9.3 ± 0.1	-1.0 ± 0.1	10.62	10.79
F2M1113+1244	0.681	Hβ	2276 ± 300	46.1	8.6 ± 0.1	0.4 ± 0.1	10.91	10.91
F2M1118−0033	0.686	Paβ	. . .	45.7	<8.7[d]	. . .	11.01	11.12
F2M1151+5359	0.780	Hα,Paβ	5700 ± 500	45.4	9.0 ± 0.1	-0.7 ± 0.1	10.48	10.88
F2M1507+3129	0.988	Hα	12800 ± 2000	45.7	9.9 ± 0.1	-1.3 ± 0.1	10.60	10.96
F2M1532+2415	0.562	Paβ	11700 ± 1000	45.6	9.8 ± 0.1	-1.2 ± 0.1	10.95	11.09
F2M1656+3821	0.732	Paβ	3064 ± 300	45.4	8.5 ± 0.1	-0.2 ± 0.1	10.54	10.67

Notes.
[a] Monochromatic luminosity at 15 μm (rest).
[b] Rest-frame B-band luminosity of the central component of the host galaxy as given in Table 6 of Urrutia et al. (2008) ("Total" host magnitude in Table 6).
[c] Rest-frame B-band luminosity of the extended host galaxy (all components) ("mono" luminosity in Table 6). The B-band luminosities were estimated from the observed I-band fluxes assuming a stellar SED flat in F_λ to perform the small k-corrections required to map observed I band to rest-frame B band.
[d] Limit on the black hole mass assuming Eddington-limited accretion.

the 70 and 160 μm photometry points alone, it has the largest uncertainties in the contribution ($\simeq 0.5$ dex). The starburst contribution ranges from $\log(L_{FIR}/L_{\odot}) = 10.67$ to 12.67, placing the host galaxies of red quasars roughly in the LIRG regime. For the QSO contribution, we find them to have bolometric luminosities in the range of $\log(L_{QSO}/L_{\odot}) = 12.03$–13.37. These are very large values, placing these quasars among the brightest in the universe in the IR furthermore strengthening our previous conclusion that we are only probing the tip of the quasar luminosity iceberg (Glikman et al. 2004, 2007; Urrutia et al. 2009).

3.3. Black Hole Masses and Accretion Rates

We estimated black hole masses (M_{BH}) for the 12 of our 13 quasars for which broad lines were visible in either the optical or near-infrared spectra (Table 3). Hβ was our preferred line as it is relatively isolated, and most quasar black hole mass estimates are calibrated on it, but in most cases the broad Hβ line was too heavily extinguished, so a longer wavelength line such as Hα or Paβ was used (Paβ was generally preferred as it is free of contaminating narrow lines). This assumed that the Hβ, Hα, and Paβ lines have the same velocity widths, but was indeed the case (within the errors) for the objects in which we could measure two or more broad-line widths (F2M0825+4716, Hα and Paβ; F2M0834+3506, Hβ and Hα; F2M0915+2418, Hα and Paβ; F2M1113+1244, Hβ, Hα, and Paβ).

Black hole mass estimates were then calculated using the broad-line widths and quasar luminosity assuming a broad-line region radius, R_{BLR}:

$$R_{BLR} = K + \alpha \log(\lambda L_\lambda(5100A)) \qquad (5)$$

(Bentz et al. 2009) with $K = -21.3$ and $\alpha = 0.519$ and estimating the intrinsic luminosity at 5500 Å, $\lambda L_\lambda(5100A)$ by measuring the quasar luminosity at a rest-frame wavelength of 15 μm (where extinction should be negligible) and applying

the ratio of the bolometric corrections at 5100 Å (12) to the correction at rest-frame 15 μm (9.0) from (Richards et al. 2006). The black hole mass estimate, M_{BH} is then given by

$$M_{BH} = f \frac{\sigma^2}{G R_{BLR}}, \qquad (6)$$

where σ is the velocity dispersion of the broad line, G is the gravitational constant, and we assume a geometric correction factor of $f = 5.5$. The Eddington luminosity is,

$$L_{Edd} = 1.3 \times 10^{31} \left(\frac{M_{BH}}{M_{\odot}} \right) W, \qquad (7)$$

and Eddington ratios are estimated by dividing the intrinsic luminosity of the quasar from the fit by the Eddington luminosity.

4. RESULTS

We first place our red quasars into the context of other LIRGs using the Spoon et al. (2007) diagnostic diagram (Figure 2). This plot of silicate absorption depth versus PAH EW separates the known classes of infrared-luminous galaxies into two. One sequence extends from region 1C (comprised mostly of starburst-dominated objects) into 1A (comprised mostly of IR-bright quasars) as continuum replaces PAH emission in objects with little silicate emission or absorption. We plot this sequence with cyan double arrows in Figure 2. The second sequence extends from 1C through 2B through 3A in which objects again become continuum dominated, but with high silicate absorption depths (the "warm ULIRG" population), shown with magenta double arrows in Figure 2.

Normal quasars are typically found in region 1A, as are the majority of our dust reddened objects, but the fact that we see one object firmly and one barely in the sparsely populated quadrant 2A of the diagram is noteworthy. Such objects are rare in most compilations of galaxies and AGNs and are believed to be part
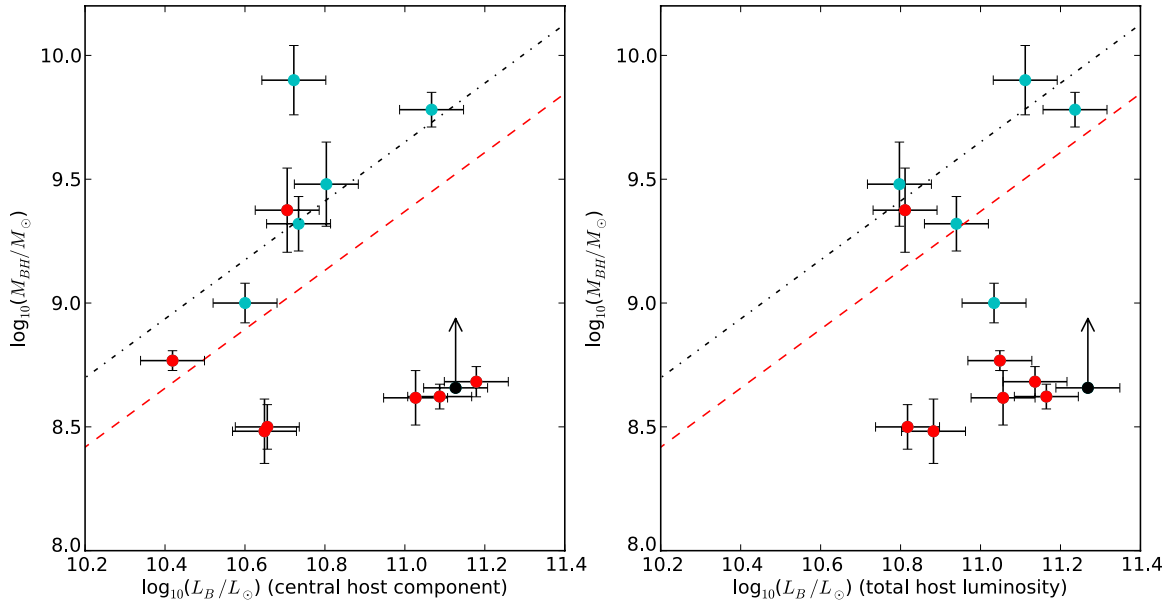
Figure 4. Black hole mass vs. host luminosity for our red quasars. Left: using the model fits to the brightest host galaxy component of Urrutia et al. (2008) and right: using the total host luminosity, including the flux in disturbed, outlying components not well fit by the model. Cyan symbols denote objects accreting at <30% of the Eddington rate, red points objects with accretion rates >30% Eddington, the object with a limit only on its black hole mass (assuming Eddington-limited accretion), F2M1118-0033, is shown as a black dot. The red dashed line is the local black hole mass–bulge luminosity relation from van der Marel (1999), the black dashed line is the relationship at $z \sim 0.7$ (interpolated from Merloni et al. 2010). Most of our high accreting object lie below the black hole mass–bulge luminosity relation.
(A color version of this figure is available in the online journal.)

of a transitioning population, confirming that we have indeed located an interesting class of object, perhaps intermediate between the heavily absorbed warm ULIRGs and the normal quasar population. Also, it is worth mentioning that none of the sources show silicate in emission, which is unusual for these very IR-bright quasars; it is possible that in some of the objects (like the four we had to fix the silicate absorption manually in the SED fitting) the silicate absorption is missing because it is being filled with an emission bump.

The results of the fitting (Figure 3 and Table 2) show that the AGN component dominates the bolometric luminosity in all cases, with most of our objects having measurements or limits on their far-infrared luminosities corresponding to star formation rates of $\sim$10–300 $M_\odot$ yr^{-1} using the Kennicutt (1998) conversion between far-infrared luminosity and star formation rate. Such star formation rates indicate luminous starbursts, but not at the level at which they are adding significantly to the stellar mass of the host galaxies.

Next we consider the accretion luminosities of our objects. Our objects span a wide range of luminosities relative to the Eddington limit ($L_{\rm Edd}$), including many objects with high luminosities when compared to typical quasar Eddington ratios $\sim$0.1 (e.g., Steinhardt & Elvis 2010). This could be an artifact of partial obscuration, for example, if the inner broad-line region, where the line widths are greatest, remains somewhat obscured. However, where we are able to measure the widths of multiple broad lines in the same object, the line widths are very similar irrespective of wavelength, making this latter possibility unlikely.

Figure 4 displays the black hole mass of our quasars versus their host luminosity, left for the central bulge component and right for the total host light. The central bulge luminosity was derived by fitting the brightest host galaxy components, while the total luminosity component included the flux in disturbed, outlying components, both after subtraction of the quasar nucleus (see Urrutia et al. 2008 for an in-depth discussion

on the AGN–host galaxy fitting). Objects with high accretion rates (above 0.3 Eddington) are plotted in red, objects with low rates in blue. The figure shows that there is very little correlation between the black hole masses and the corresponding galaxy luminosities, either of the fitted central galaxy component or to the total host galaxy light. However, none of our black hole masses exceed the black hole mass–bulge luminosity relation (Marconi & Hunt 2003) by a large factor, also when corrected for evolution according to Bennert et al. (2010), even when only the central component of a merging system (defined as the one containing the quasar nucleus) is considered. The fact that we find a significant fraction of our objects with high accretion rates below the black hole mass–bulge luminosity relation leads us to speculate that they are young, just ignited black holes. Their growth has started after the host galaxy growth via a starburst event, yet since they are accreting at such high rates they will move onto the "classical" relation within $\sim$10^7 years.

In Figure 5, we plot both the total FIR luminosity against the AGN luminosity, and the ratio of accretion rate to the Eddington limit of the quasar against the ratio of the far-infrared luminosity to the B-band luminosity of the host galaxy (a proxy for the specific star formation rate). There is a hint of a correlation between the total FIR luminosity and AGN luminosity (as found for nearby quasars; Netzer et al. 2007), though it is not tight. There seems to be no relation between the mass-normalized quantities of specific star formation rate and accretion rate relative to the Eddington limit.

Finally, in Figure 6, we examine the relationship between the host galaxy morphology and the star formation rate and AGN accretion rate. In order to quantify the degree of disturbance of the host we use the ratio of Gini coefficient (G) to concentration index (C). We showed in Urrutia et al. (2008) that the combination of these two quantities gave a robust indication of the degree of disturbance of the host galaxy. We therefore define a "disturbance parameter," $D = G/C$. This quantity is
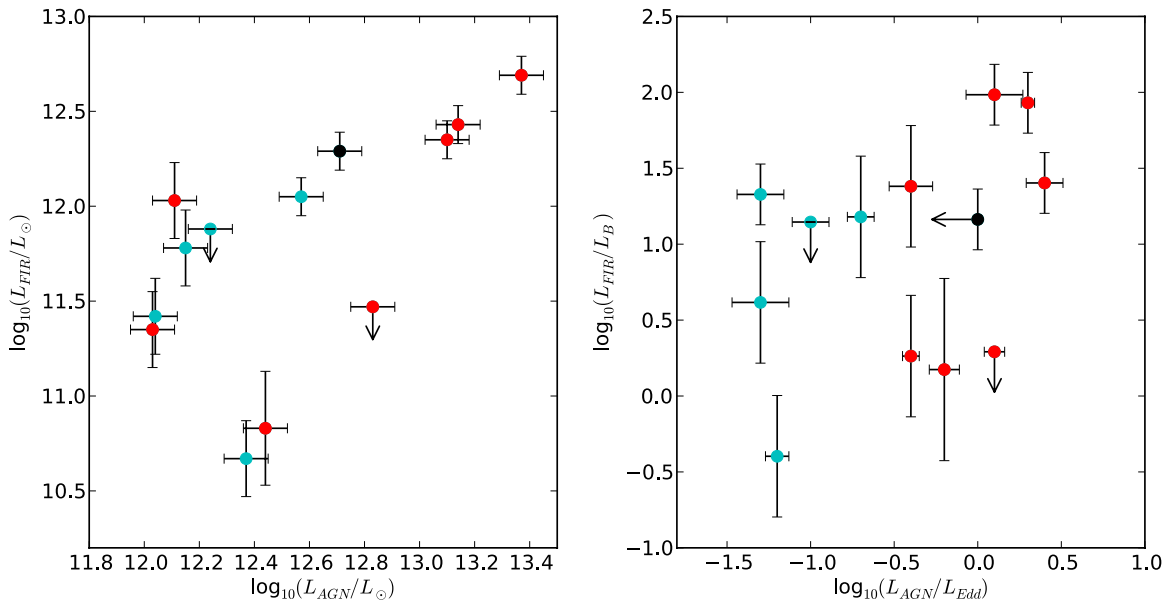
Figure 5. Log of the ratio of far-infrared luminosity to host luminosity in *B* band (as a proxy for the specific star formation rate) is plotted against the accretion rate relative to the Eddington limit. Symbols are as in Figure 4. While the most luminous quasars also show the highest luminosity in the FIR, there is no correlation between the inferred star formation and accretion rate of the quasar.
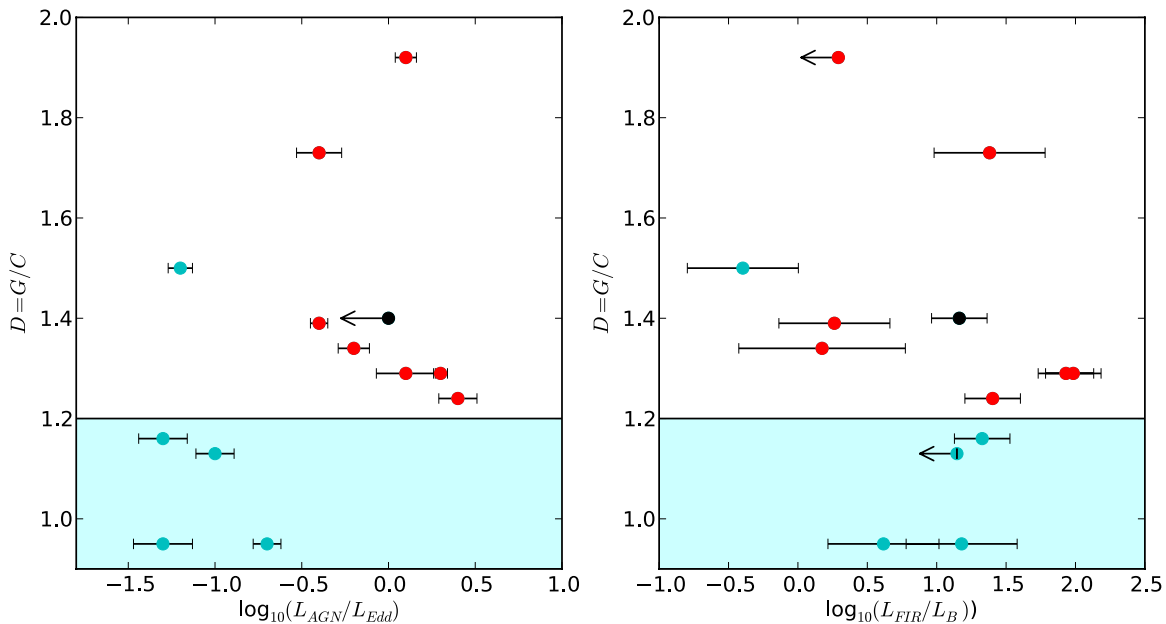
(A color version of this figure is available in the online journal.)

Figure 6. Right: host galaxy morphological distortion, parameterized as *D*, the ratio of the Gini coefficient (*G*) to the concentration index (*C*) against Eddington ratio. Normal galaxies have a mean $D \approx 1.2$ (Abraham et al. 2003), objects with values below this (shaded in the plot) are relatively undisturbed, those with higher values have increasing amounts of disturbance. Symbol colors as for Figure 4. Left: morphological distortion vs. the log of the ratio of far-infrared luminosity to host luminosity in *B* band, an indicator for star formation. While there could be a hint of a correlation between the amount of host disturbance and the accretion rate, there is no correlation found for star formation vs. the host disturbance.

(A color version of this figure is available in the online journal.)

approximately unity for normal galaxies (Abraham et al. 2003), but is significantly greater than unity for highly disturbed systems. There is a weak (though not statistically significant) trend for high accretion rate objects to have more disturbed morphologies, though there is no apparent trend with specific star formation rate.

5. DISCUSSION

Our aim in this study was to determine whether the infrared properties of these dust reddened objects were consistent with the merger-driven co-evolutionary model for the growth of supermassive black hole and their host galaxies. In particular, whether these objects are an intermediate stage between a merger-induced starburst and a "normal" quasar with an unreddened, blue continuum, with AGN feedback having stopped further star formation in the host. Our results seem to be consistent with this overall picture, but we see considerable variation in properties such as silicate absorption depth, star formation rate, and AGN accretion rate on an object-by-object basis.

Much of the object-to-object variation is due to the heterogeneity of our sample; some have high reddenings,

morphological disturbances, some do not. While they all are luminous quasars, they do span a large range in luminosities, too. In the overall picture, however, trends are evident. If an object is morphologically disturbed, it is much more likely to have a high Eddington ratio and to show silicate in absorption (be reddened by cold dust). Similarly, the two quasars which did not show any signs of merger interaction in Urrutia et al. (2008) also do not display high Eddington ratios or silicate in absorption and therefore should not be included with the characterization as "young quasars." Not all dust obscured quasars fit in the co-evolutionary scenario, but statistically, it is the most likely explanation and therefore our conclusions are to be taken as such.

All these objects have mid-infrared (AGN) luminosities in excess of their far-infrared (presumed starburst) luminosities. This dominance of the AGN suggests that AGN feedback processes, if they are indeed important, will have started to have their impact on star formation in the host galaxy as we would have expected the starburst component to have dominated otherwise. We do not see any obvious quasar feedback "smoking guns;" broad absorption line features from AGN thermal winds, for example, are not present in any of our objects which are of high enough redshift to see Mg II absorption ($z \gtrsim 0.7$). However, experience from Urrutia et al. (2009) has shown that for the red quasars selected using our criteria the spectrum below ≈ 5000 Å is so extinguished that even deep absorption features are difficult to detect in objects with $z \lesssim 0.9$. Only three of our objects (F2M0729+3336, F2M1012+2825, and F2M1507+3129) have appropriate redshifts, and F2M0729+3336 is too noisy to detect absorption features. Nevertheless, an excess of low-ionization, broad absorption line quasars has been found in our full sample of red quasars (Urrutia et al. 2009) and a tentative relationship between wind properties and star formation has been seen by Farrah et al. (2012) in samples of reddened quasars.

Blueshifted wings to [O III]5007 Å with velocities relative to the line peak of up to ~1000 km s^{-1} are seen in 5 of our 13 objects (F2M0729+3336, F2M0825+4716, F2M0915+2418, F2M1118−0033, and F2M1151+5359). Of the four of these for which we can estimate accretion rates, three have accretion rates just exceeding the Eddington limit, possibly indicating a link with extremely high accretion rates, but the star formation rates in the hosts vary widely. We also lack any information on the spatial extent of these outflows, which may be confined to the nuclear regions. Blueshifted [O III] line components are common in compact radio sources: Holt et al. (2008) propose that these components are due to outflows of gas driven by the radio jets. The radio sources in our quasars are however significantly less luminous than those in the radio galaxies studied by Holt et al. (2008). Radio-quiet type-2 luminous quasars at low redshift also tend to show outflows in [O III]5007 Å emission (Greene et al. 2011), suggesting that these are not confined to radio sources, though the most spectacular object in the Greene et al. (2011) sample, J1356+1026, is a relatively strong radio source (Greene et al. 2012). Clearly the role of radio jets in powering these outflows needs to be established.

In agreement with the evolutionary model, we see a large fraction of objects with high black hole accretion rates, consistent with the idea that quasar accretion rates are high in the early phase of growth. The objects with the highest accretion rates also tend to fall below the local black hole mass–bulge luminosity relation by ~0.5 dex; none of our objects with lower accretion rates are found there. This offset from the local relation is consistent with a picture in which the black hole is yet to grow to its equilibrium size following a major merger. It is also broadly consistent with numerical simulations of black hole growth in quasar merger scenarios, in which the total black mass hole grows by about 0.5 dex with every major merger event (e.g., Li et al. 2007, Figure 10). Sarria et al. (2010) also find that their luminous, dust obscured quasars at $z \sim 2$ fall below the black hole mass–bulge mass relation at that redshift. An interesting exception is F2M0915+2418, which has a high accretion rate, but falls close to the black hole mass–bulge mass relation. This object also has one of the highest star formation rates in the sample, however, allowing it to evolve along a trajectory that will keep it close to the black hole mass–bulge mass relation.

We do, however, have some remaining puzzles, where our data do not fit in with the most naive expectations of the evolutionary model. In Urrutia et al. (2008) we saw a relationship between D and the amount of reddening in the host, but in Figure 6 there seems to be little correlation between the degree of disturbance of the host galaxy and the star formation rate, except that all high accreting quasars are also disturbed to some degree. There may, however, be a very weak trend for objects with high accretion rates relative to the Eddington limit to have high values of D, see Figure 6. Similarly, there is no clear morphological trend related to the offset of the quasar from the local galaxy luminosity–black hole mass relation.

To some extent, the lack of clear trends here may be due to an admixture of objects reddened by foreground galaxies. In particular, the low accretion rate objects may include some objects where the reddening is from an intervening galaxy through a chance alignment, perhaps from a galaxy in the same group or cluster. F2M1532+2415 is a good example of this, with an apparently highly disturbed, early stage merger morphology, but both a low accretion rate and a low star formation rate, and F2M0834+3506 is a very good candidate for a low accretion rate broad-line radio galaxy reddened by a foreground irregular galaxy.

In summary, our observations are consistent with the simplest evolutionary models, where a merger-induced starburst triggers an obscured quasar which begins life accreting at close to the Eddington rate and later evolves into an unobscured quasar accreting at the ~0.1 of the Eddington rate more typically observed in the normal quasar population. We see no obvious evidence, however, of feedback affecting star formation in this particular sample (though we do see evidence of strong outflows of ionized gas in some objects). Nor do we see a clear sequence or progression from a newborn, highly obscured, high accretion rate AGN with a very disturbed host into a quiescent, almost unreddened object with a lower accretion rate. Our quasars were, however, selected within a fairly narrow range of luminosity (due to the 2MASS detection requirement and restricted redshift range) and reddening (if the reddening were too high, they would be classed as type-2s, but if it were too low they would not be picked out as red quasars), so we might not expect to be able to see much of an evolutionary sequence.

These observations are most consistent with a picture in which the majority of objects undergo the starburst/merger phase well before we see these reddened quasars emerge, though not so long after that evidence for morphological disturbance of the hosts has been erased. The evolution in the black hole mass–bulge mass plane is then a shift along the bulge mass axis by ~ +0.5 dex followed ~10^8 yr later by a shift along the black hole mass axis by a similar amount. In one case, however, (F2M0915+2418) we do seem to see the starburst and accretion happening simultaneously. As our selection techniques for

the dust reddened quasar population expand, particularly as mid-infrared-selected samples become large enough to include significant numbers of reddened type-1 quasars we expect to be able to expand our samples considerably and trace out more of the evolutionary scenario.

APPENDIX

NOTES ON INDIVIDUAL OBJECTS

A.1. F2M0729+3336

This object lies outside the SDSS coverage, so photometry from the ESI spectrum was used when constructing the SED. Both the silicate feature and the optical SED are well fit with a reddening of $E(B - V) = 0.83 \pm 0.22$. The object is detected in the X-ray by *Chandra* with six hard X-ray photons (Urrutia et al. 2005). It has an accretion rate close to (formally slightly in excess of) the Eddington limit, but no evidence of cool dust from substantial star formation activity, though the host galaxy appears disturbed. The inferred black hole mass lies significantly below the black hole mass–bulge luminosity relation consistent with our observation that the black hole is still growing rapidly.

A.2. F2M0825+4716

Another high accretion rate object, but this one also has a strong starburst component in the far-infrared. The host is very disturbed, but, if the fit to the central component of the galaxy only is considered, lies close to the black hole mass–bulge luminosity relation. The strong black hole growth would thus take it significantly above the relation within a Salpeter time, if it was not for the high star formation rate, and the likelihood that some of the extended components of the host galaxy would merge with the central one in that timescale. As such, F2M0825+4816 is a prime example of black hole–host galaxy co-evolution.

A.3. F2M0830+3759

The lowest redshift ($z = 0.414$) object in our sample, with a strong *Chandra* detection (Urrutia et al. 2005). A deeper X-ray spectrum with *XMM* reveals a cold or only moderately ionized absorber with a column density consistent with it being associated with the dust causing the quasar reddening, as well as an Fe Kα emission line from a reflection component (Piconcelli et al. 2010). This object has a relatively massive host galaxy, and the object lies below the black hole mass–bulge luminosity relation. Nevertheless, the accretion rate is relatively high $L/L_{\mathrm{Edd}} \approx 0.4$, so again, this quasar may be able to build black hole mass effectively. The star formation rate is constrained to be relatively low, $\sim 10 \ M_{\odot} \ \mathrm{yr}^{-1}$.

A.4. F2M0834+3506

This object has little or no silicate absorption, inconsistent with the observed reddening in the optical. The *HST*/ACS image too suggests that this, rather than being a post-merger system, may be a normal quasar obscured by a foreground irregular galaxy. The spectrum shows multiple-peaked permitted lines, with three identifiable components, one at the same redshift as the forbidden lines, one at $\approx +3600 \ \mathrm{km \ s}^{-1}$ and one at $\approx -5100 \ \mathrm{km \ s}^{-1}$. The object is the only one of two in our sample to show multiple-peaked permitted lines, typically only seen in low accretion rate, radio-loud objects (Eracleous & Halpern 2003), and our analysis indeed confirms a low accretion rate and a relatively low star formation rate. It lies a little above the local black hole mass–bulge luminosity relation, consistent with the idea that this object is a fairly normal quasar obscured by dust from a foreground object.

A.5. F2M0841+3604

Consistent with the very irregular morphology, this object is well fit by the simple cold dust screen model. It has both a moderately high accretion rate and moderately high star formation rate, lying below the black hole mass–bulge luminosity relation. The radio information reveal a steep spectrum point source, while the X-ray image shows a very high hardness ratio (Urrutia et al. 2005).

A.6. F2M0915+2418

This object is the most luminous quasar in our sample and is bright enough in the infrared to be detected in the IRAS Faint Source Catalog. The IRS spectrum is an archival one from Sargsyan et al. (2008). This object has both a high star formation rate and high accretion rate and is the only one of our high accretion rate objects to fall close to the black hole mass–bulge mass relation in both plots of Figure 4. Due to its high star formation rate and high accretion rate, it will evolve with a trajectory close to the black hole mass–bulge mass relation for at least a Salpeter time ($\sim 10^8$ yr).

A.7. F2M1012+2825

A fairly unexceptional object in terms of its accretion rate, star formation rate, and position on the black hole mass–bulge luminosity relation, it does, however have a double nucleus with a separation of only 1.2 kpc (Urrutia et al. 2008).

A.8. F2M1113+1244

Another good candidate for a young quasar, with a high accretion rate (super Eddington; $\log(L/L_{\mathrm{Edd}}) = 0.4 \pm 0.1$),
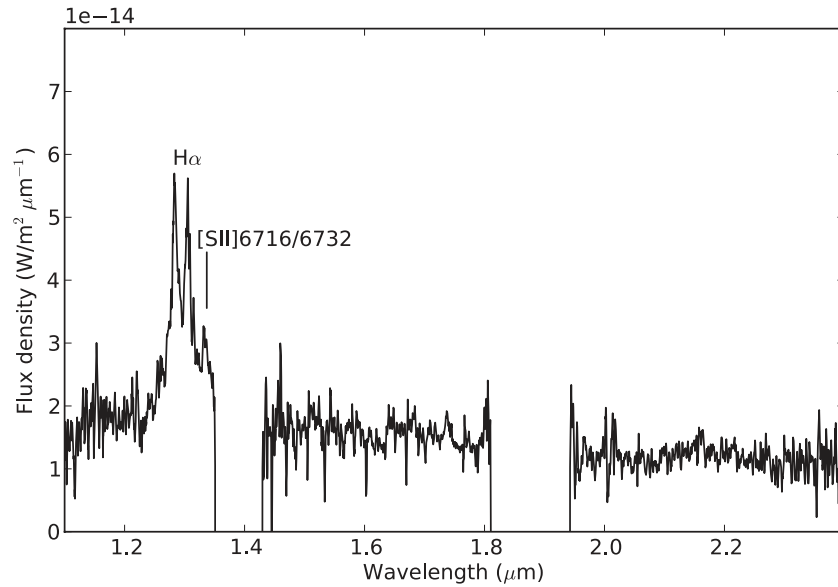
Figure 7. Near-infrared spectrum of F2M1507+3129 showing a double-peaked Hα line.

high star formation rate (FIR contribution in ULIRG regime; $\log(L_{\mathrm{FIR}}/L_\odot) = 12.39$), and plotting well below the black hole mass–bulge mass relation.

A.9. F2M1118−0033

This object shows no clear broad lines in either the optical or near-infrared spectrum. Hα is detected, but is relatively narrow ($\approx 1000\,\mathrm{km\,s^{-1}}$). There is a hint of broad Paβ in the near-infrared K band, but it is not strong enough to allow us to estimate a line width. The SED is consistent with a reddened quasar. No black hole mass estimate is possible in this case, though we have obtained a limit based on the quasar luminosity and assuming Eddington-limited accretion.

A.10. F2M1151+5359

The reddening of this quasar is relatively modest, and the host almost undisturbed. Nevertheless, it has a high accretion rate and relatively high star formation rate and lies well below the black hole mass–bulge mass relation.

A.11. F2M1507+3129

This object has a near-infrared spectrum in Glikman et al. (2004); however, we obtained an improved near-infrared spectrum with the Triplespec instrument (Herter et al. 2008) on the Hale 200 inch telescope on 2011 July 11. The data were calibrated using the A0V star HD127304. The new spectrum clearly shows a double-peaked broad Hα emission line in J band (Figure 7). The object is the second highest redshift double-peaked quasar currently known and is more luminous than CXOECDFSJ0331-2755 at $z = 1.369$, the most distant double-peaked emitter (Luo et al. 2009). Like many objects in this class (Lewis & Eracleous 2006), and indeed similar to the other double-peaked emitter in our sample, F2M0834+3506, it has a relatively low accretion rate (0.05 Eddington).

A.12. F2M1532+2415

The SED of this object is difficult to fit, consistent with the complicated structure seen in the host galaxy image. Despite a red continuum, the IRS spectrum lacks silicate absorption. The

far-infrared luminosity is very low, the accretion rate is also low, and the object lies close to the black hole mass–bulge mass relation. As of now the underlying physics responsible for the reddening and host disturbance is difficult to explain.

A.13. F2M1656+3821

This object has a relatively low star formation rate (barely above the LIRG regime; $\log(L_{\mathrm{FIR}}/L_\odot) = 11.19$), but a high accretion rate (roughly Eddington rate) and should be able to accrete matter onto the black hole to move up to the black hole mass–bulge mass relation from its current position ≈ 0.5 dex below. It is also the object that is clearly in quadrant 2A of the Spoon et al. (2007) diagram, since it has such a deep silicate absorption feature.

REFERENCES

Abraham, R. G., van den Bergh, S., & Nair, P. 2003, ApJ, 588, 218
Alonso-Herrero, A., Pérez-González, P. G., Alexander, D. M., et al. 2006, ApJ, 640, 167
Antonucci, R. 1993, ARA&A, 31, 473
Becker, R. H., White, R. L., & Helfand, D. J. 1995, ApJ, 450, 559
Bennert, N., Canalizo, G., Jungwiert, B., et al. 2008, ApJ, 677, 846
Bennert, V. N., Treu, T., Woo, J.-H., et al. 2010, ApJ, 708, 1507
Bentz, M. C., Peterson, B. M., Netzer, H., Pogge, R. W., & Vestergaard, M. 2009, ApJ, 697, 160
Chiar, J. E., & Tielens, A. G. G. M. 2006, ApJ, 637, 774
Cutri, R. M., Nelson, B. O., Kirkpatrick, J. D., Huchra, J. P., & Smith, P. S. 2001, in ASP Conf. Ser. 232, The New Era of Wide Field Astronomy, ed. R. G. Clowes, A. J. Adamson, & G. E. Bromage (San Francisco, CA: ASP), 78
Donley, J. L., Rieke, G. H., Pérez-González, P. G., & Barro, G. 2008, ApJ, 687, 111
Donley, J. L., Rieke, G. H., Pérez-González, P. G., Rigby, J. R., & Alonso-Herrero, A. 2007, ApJ, 660, 167
Donley, J. L., Rieke, G. H., Rigby, J. R., & Pérez-González, P. G. 2005, ApJ, 634, 169
Dunne, L., & Eales, S. A. 2001, MNRAS, 327, 697
Eracleous, M., & Halpern, J. P. 2003, ApJ, 599, 886
Farrah, D., Urrutia, T., Lacy, M., et al. 2012, ApJ, 745, 178
Ferrarese, L., & Merritt, D. 2000, ApJ, 539, 9
Georgakakis, A., Clements, D. L., Bendo, G., et al. 2009, MNRAS, 394, 533
Glikman, E., Gregg, M. D., Lacy, M., et al. 2004, ApJ, 607, 60
Glikman, E., Helfand, D. J., & White, R. L. 2006, ApJ, 640, 579
Glikman, E., Helfand, D. J., White, R. L., et al. 2007, ApJ, 667, 673

Glikman, E., Urrutia, T., Lacy, M., et al. 2012, ApJ, 757, 51
Greene, J. E., Zakamska, N. L., Ho, L. C., & Barth, A. 2011, ApJ, 732, 9
Greene, J. E., Zakamska, N. L., & Smith, P. S. 2012, ApJ, 746, 86
Gregg, M. D., Lacy, M., White, R. L., et al. 2002, ApJ, 564, 133
Hao, L., Spoon, H. W. W., Sloan, G. C., et al. 2005, 625, 75
Hao, L., Weedman, D. W., Spoon, H. W. W., et al. 2007, ApJ, 655, 77
Herter, T. L., Henderson, C. P., Wilson, J. C., et al. 2008, Proc. SPIE, 7014, 30
Hickox, R. C., Jones, C., Forman, W. R., et al. 2007, ApJ, 671, 1365
Hickox, R. C., Jones, C., Forman, W. R., et al. 2009, ApJ, 696, 891
Hiner, K. D., Canalizo, G., Lacy, M., et al. 2009, ApJ, 706, 508
Holt, J., Tadhunter, C. N., & Morganti, R. 2008, MNRAS, 387, 639
Hopkins, P. F., Hernquist, L., Cox, T. J., & Kereš, D. 2008, ApJS, 175, 356
Houck, J. R., Roellig, T. L., van Cleve, J., et al. 2004, ApJS, 154, 18
Kartaltepe, J. S., Sanders, D. B., Le Floc'h, E., et al. 2010a, ApJ, 709, 572
Kartaltepe, J. S., Sanders, D. B., Le Floc'h, E., et al. 2010b, ApJ, 721, 98
Kennicutt, R. C. 1998, ARA&A, 36, 189
Lacy, M., Gregg, M. D., Becker, R. H., et al. 2002, AJ, 123, 2925
Lacy, M., Petric, A. O., Sajina, A., et al. 2007, AJ, 133, 186
Lacy, M., Sajina, A., Petric, A. O., et al. 2007, ApJ, 669, 61
Lacy, M., Storrie-Lombardi, L. J., Sajina, A., et al. 2004, ApJS, 154, 166
Lewis, K. T., & Eracleous, M. 2006, ApJ, 642, 711
Li, Y., Hernquist, L., Robertson, B., et al. 2007, ApJ, 665, 187
Lotz, J. M., Primack, J., & Madau, P. 2004, AJ, 128, 163
Luo, B., Brandt, W. N., Silverman, J. D., et al. 2009, ApJ, 695, 1227
Magorrian, J., Tremaine, S., Richstone, D., et al. 1998, AJ, 115, 2285
Marconi, A., & Hunt, L. K. 2003, ApJ, 589, 21
Martínez-Sansigre, A., Lacy, M., Sajina, A., & Rawlings, S. 2008, ApJ, 674, 676
Martínez-Sansigre, A., Rawlings, S., Lacy, M., et al. 2005, Nature, 436, 666
Merloni, A., Bongiorno, A., Bolzonella, M., et al. 2010, ApJ, 708, 137
Mor, R., & Trakhtenbrot, B. 2011, ApJ, 737, L36
Netzer, H., Lutz, D., Schweitzer, M., et al. 2007, ApJ, 666, 806

Nikutta, R., Elitzur, M., & Lacy, M. 2009, ApJ, 707, 1550
Piconcelli, E., Vignali, C., Bianchi, S., et al. 2010, ApJ, 710, 992
Richards, G. T., Lacy, M., Storrie-Lombardi, L. J., et al. 2006, ApJS, 166, 470
Rieke, G. H., Young, E. T., Engelbracht, C. W., et al. 2004, ApJS, 154, 25
Sajina, A., Scott, D., Dennefeld, M., et al. 2006, MNRAS, 369, 939
Sanders, D. B., & Mirabel, I. F. 1996, ARA&A, 34, 749
Sargsyan, L., Mickaelian, A., Weedman, D., & Houck, J. 2008, ApJ, 683, 114
Sarria, J. E., Maiolino, R., La Franca, F., et al. 2010, A&A, 522, 3
Schweitzer, M., Lutz, D., Sturm, E., et al. 2006, ApJ, 649, 79
Shi, Y., Rieke, G. H., Ogle, P., Jiang, L., & Diamond-Stanic, A. M. 2009, ApJ, 703, 1107
Siebenmorgen, R., Haas, M., Krügel, E., & Schulz, B. 2005, A&A, 436, 5
Silk, J., & Rees, M. J. 1998, A&A, 331, 1
Skrutskie, M. F., Cutri, R. M., Stiening, R., et al. 2006, AJ, 131, 1163
Spoon, H. W. W., Marshall, J. A., Houck, J. R., et al. 2007, ApJ, 654, 49
Steinhardt, C. L., & Elvis, M. 2010, MNRAS, 402, 2637
Stern, D., Eisenhardt, P., Gorjian, V., et al. 2005, ApJ, 631, 163
Sturm, E., Hasinger, G., Lehmann, I., et al. 2006, ApJ, 642, 81
Urrutia, T., Becker, R. H., White, R. L., et al. 2009, ApJ, 698, 1095
Urrutia, T., Lacy, M., & Becker, R. 2008, ApJ, 674, 80
Urrutia, T., Lacy, M., Gregg, M. D., & Becker, R. H. 2005, ApJ, 627, 75
Urry, C. M., & Padovani, P. 1995, PASP, 107, 803
Vanden Berk, D. E., Richards, G. T., Bauer, A., et al. 2001, AJ, 122, 549
van der Marel, R. P. 1999, AJ, 117, 744
Werner, M. W., Roellig, T. L., Low, F. J., et al. 2004, ApJS, 154, 1
White, R. L., Helfand, D. J., Becker, R. H., et al. 2003, AJ, 126, 706
Wright, E. L., Eisenhardt, P. R. M., Mainzer, A. K., et al. 2010, AJ, 140, 1868
Zakamska, N. L., Gómez, L., Strauss, M. A., & Krolik, J. H. 2008, AJ, 136, 1607
Zakamska, N. L., Strauss, M. A., Krolik, J. H., et al. 2003, AJ, 126, 2125